Received: 14 November 2022 | Revised: 1 March 2023 | Accepted: 17 April 2023

DOI: 10.1002/nag.3547

RESEARCH ARTICLE

WILEY

Modelling the density homogenisation of a block and granular bentonite buffer upon non-isothermal saturation

Jose A. Bosch[1] | **Alessio Ferrari**[1,2] | **Olivier Leupin**[3] | **Lyesse Laloui**[1]

[1]École Polytechnique Fédérale de Lausanne, EPFL, Lausanne, Switzerland

[2]Dipartimento di Ingegneria, Università degli Studi di Palermo, Palermo, Italy

[3]Nagra, National Cooperative for the Disposal of Radioactive Waste, Wettingen, Switzerland

Correspondence
Jose A. Bosch, École Polytechnique Fédérale de Lausanne, EPFL, Station 18, CH-1015 Lausanne, Switzerland.
Email: jose.boschllufriu@epfl.ch

Abstract

This paper presents a numerical analysis of the mechanical performance of a bentonite clay buffer for the containment of nuclear waste in the context of deep geological disposal. The design of the buffer is based on the Swiss concept where the waste canisters are emplaced on pedestals of compacted bentonite blocks and the remaining space between the tunnel and the canister is backfilled with grains of highly compacted bentonite. A complete analysis of the long-term performance of the repository requires a good understanding of the mechanical evolution of the bentonite upon heating from the radioactive waste and hydration from the host rock. Despite its importance, the implications of the initial heterogeneous bentonite layout, characterised by blocks and grains, on the final dry density at the repository scale in the steady state have not been previously studied. The present study aims to shed light into these processes by means of finite element modelling using an advanced constitutive model for the bentonite behaviour that considers several thermo-hydro-mechanical couplings. The constitutive model is shown to be able to reproduce several laboratory tests involving saturation of block and pellets at different dry densities. The model predictions, extended up to 100,000 years, indicate that the bentonite blocks and grains tend to homogenise in terms of dry density as the buffer reaches full saturation. Due to the different swelling potential of the block pedestal and the granular backfill, the canister is subjected to movements, although these remain relatively small. The impact of initial segregation of the granular bentonite is also studied and it is seen to not to affect substantially the mechanical evolution of the buffer, although it might reduce canister displacements.

KEYWORDS

bentonite, heterogeneity, nuclear waste, thermo-hydro-mechanical couplings, unsaturated soils

1 | INTRODUCTION

Many designs of deep geological repositories for high level radioactive waste (HLW) involve the use of bentonite as backfill and sealing material of tunnels and galleries where the waste will be emplaced. As a result of different functions that bentonite has to fulfil, while ensuring relatively easy emplacement, some designs envisage the emplacement of bentonite in different forms and layouts.[1] Some examples include the SKB concept in Sweden and Finland in which block bentonite will be used as a buffer between the crystalline rock and the nuclear waste canisters (Borgesson[2], SKB[3]) and the CIGEO concept in France in which bentonite mixtures (such as compacted pellets and crushed claystone produced from the repository excavation) will be used to seal the access galleries to the disposal boreholes.[4,5] In the Swiss concept of repository, the canister will be supported by a pedestal of bentonite blocks and the remaining space between the canister and the tunnel will be filled by a granular bentonite mixture (GBM). The bentonite pedestal will provide support for the canisters in the early stages, while the granular bentonite allows to optimise the backfilling operation.[6] This disposition of block-GBM results in an inherently initially heterogeneous buffer, whose heterogeneity could be accentuated by the possible segregation of GBM during the backfilling operation.[7]

Since the main safety functions of bentonite, such as swelling pressure and hydraulic conductivity, depend on its dry density,[8,9,10–12] the design of the system requires an understanding of the effects of the initial heterogeneous disposition on the performance of the overall buffer, ensuring for instance that upon saturation the two forms of bentonite will tend to homogenise as it has been observed in laboratory experiments.[13–15] This homogenisation would avoid preferential flow paths for water flowing from the host rock or gas generated from canister corrosion. Another consequence of the heterogeneous bentonite relates to canister movements induced by the differential swelling pressure of the block and GBM as a result of the different initial dry density.[16] Hydraulic conductivity and thermal conductivity of the two materials are also different, thereby further differences in behaviour between the two materials in early stages are expected.

Although many studies have investigated the THM performance of different repository concepts in the short and long term (Gens et al.[17] Dupray et al.,[18] Zheng et al.[19]), the mechanical evolution of the bentonite buffer, such as swelling pressure and dry density, is usually either simplified or not reported.[20] In addition, while most of these studies have been devoted to the analysis of block bentonite buffers, mainly driven by the large amount and quality of data provided by the FEBEX test,[18,21,22] very few modelling efforts have been directed towards the Thermo-Hydro-Mechanical (THM) analysis of buffers involving GBM in addition to bentonite blocks. Among them, Alonso and Hoffmann[23] modelled the EB experiment that involved artificial hydration under isothermal conditions of a block-GBM buffer, and Dupray and Laloui[24] studied numerically the movement of the canister induced by the THM evolution of a buffer representative of the Swiss concept. However, no specific conclusions were drawn in these studies regarding the spatial evolution of the dry density. In a recent numerical benchmark, Gens et al.[25] concluded that further research is needed to elucidate the causes of redistribution of bentonite density upon saturation.

The present study aims to advance towards understanding the mechanical interaction between bentonites emplaced at different dry densities, such as blocks and GBM, and to provide new insights on their mechanical homogenisation upon saturation in terms of dry density and swelling pressure. The core of the analyses is the application of a recent THM constitutive model especially suitable for the mechanical evolution of bentonite from unsaturated to saturated states including non-isothermal conditions.[26] This has been implemented in the finite element code LAGAMINE[27] and has been used to perform the analyses. The focus of the study lies on the buffer, without considering mechanical interaction with the tunnel liner and host-rock, which are included in the simulations in order to obtain meaningful thermo-hydraulic boundary conditions for the bentonite buffer.

The paper starts by reviewing full scale experiments regarding block and GBM buffers under both isothermal (EB-experiment[16]) and non-isothermal (FE-experiment[30]) conditions, which motivates the present study. Afterwards, the numerical framework used for the analysis is described, as well as the finite element model set up, which is largely based on the FE experiment. The calibration of material parameters plays a central role in providing reliable predictions, and accordingly a specific calibration strategy for bentonite compacted at different dry densities is outlined based on recent interpretations, in particular, that the saturated state behaviour of bentonite does not depend on its as-compacted state.[26,28] The suitability of the constitutive model for reproducing bentonite behaviour is demonstrated by simulating experimental tests at the laboratory scale within the range of dry densities used in the buffer.

The THM finite element simulations were performed up to 100,000 years and two cases of initial dry density distribution in the buffer were analysed. A base case is considered in which the GBM has a uniform distribution of dry density. A heterogeneous distribution of GBM density is studied for the first time with the alternative case, based on observations from

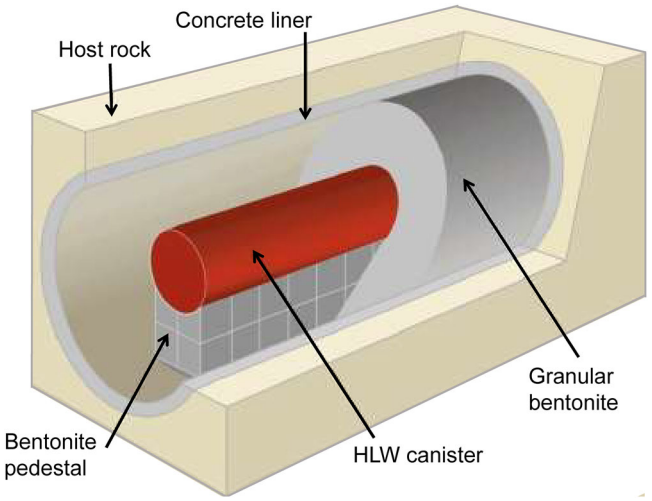

FIGURE 1 Schematic representation of the buffer components in the Swiss concept of deep geological repository. HLW stands for high level radioactive waste (modified from NAGRA[31]).

a full-scale emplacement experiment,[7,29] in order to assess the consequences of GBM segregation during its emplacement on the capacity of the buffer to homogenise.

2 | BACKGROUND

The repository design, that is, analysed in this work corresponds to the Swiss concept for high-level radioactive waste disposal. A schematic view of the bentonite buffer design is shown in Figure 1, that includes the canister supported by a bentonite pedestal and the GBM backfill.[31] The tunnels will be excavated at high depth in the Opalinus Clay formation, which will act as a geological barrier, and a concrete liner will be installed to ensure tunnel stability at early stages. Over time, as bentonite hydrates, mechanical stability will be further ensured by the swelling pressure developed by the bentonite buffer.

Large scale tests have been performed in order to assess the technical feasibility and performance of bentonite buffers using similar dispositions. The EB Experiment, reported in Mayor et al.,[16] demonstrated the feasibility and advantages of using GBM as buffer material in order to optimise the backfill procedure. In that experiment the buffer was artificially hydrated under isothermal conditions, in order to reach full saturation in less than 10 years. Upon dismantling of the test, it was verified that the bentonite blocks and GBM reached a relatively homogeneous state in terms of dry density.[32] Based on lessons learned from the EB experiment, a new backfilling machine was designed and tested in an emplacement test, which demonstrated the feasibility of achieving a target dry density of at least 1.45 Mg/m^3 for the overall GBM backfill,[7] with local values derived from CPT measurements between 1.4 and 1.6 Mg/m^3.

Since 2014, the Full-Scale Emplacement (FE) experiment in the Mont-Terri rock laboratory[30] has been under operation with the aim of verifying the construction feasibility and to further understand repository-induced THM effects on the buffer and host-rock. Accordingly, it involves natural hydration and artificial heating. After 5 years of operation a settlement of the heaters of around 10 mm had been observed,[31] which is in the opposite trend that was measured from the EB experiment, where an upward movement of the dummy steel canister was registered.[16] The latter result was expected, due to the different swelling potential between the pedestal and the GBM, and the initial settlement observed in the FE experiment is analysed in the present work.

3 | MODELLING FRAMEWORK

3.1 | THM formulation

The THM coupled formulation used in this work is described in detail in Collin[33] and a variety of relevant applications are reported in Collin et al.[34,35] For the sake of conciseness only a summary is given in the following. The equations are

formulated based on the theory of mixtures following the compositional approach.[36] The balance equations are established in terms of three species that are solid, water and dry air; and four primary state variables that are water pressure p_w, gas pressure p_g, temperature T and the displacement vector $\mathbf{u}$.

The equations are derived considering large deformations using an updated Lagrangian formulation.[27,35] Changes in porosity, n in a volume of mixture V, are computed from the mass balance of solids in the current configuration:

$$\frac{\partial}{\partial t}[\rho_s(1-n)V] = 0 \tag{1}$$

where ρ refers to density and the subscript s to the solid species. The mass conservation equations for the water (subscript w) and dry air (subscript a) species are, respectively:

$$\frac{\partial}{\partial t}(\rho_w n S_r) + \mathrm{div}(\rho_w \mathbf{f}_l) - Q_w + \frac{\partial}{\partial t}[\rho_v n(1-S_r)] + \mathrm{div}(\mathbf{i}_v + \rho_v \mathbf{f}_g) - Q_v = 0 \tag{2}$$

$$\frac{\partial}{\partial t}[\rho_a n(1-S_r)] + \mathrm{div}(\mathbf{i}_a + \rho_a \mathbf{f}_g) - Q_a + \frac{\partial}{\partial t}(H\rho_a n S_r) + \mathrm{div}(H\rho_a \mathbf{f}_l) - Q_{da} = 0 \tag{3}$$

where the subscript l stands for liquid phase, the subscript v stands for vapor phase, the subscript a for dry air and the subscript da for dissolved air in the liquid phase, $\mathbf{f}$ indicates advective fluxes, $\mathbf{i}$ diffusive fluxes, Q stands for the external sources and H refers to the Henry constant which indicates the proportion of dissolved air in the liquid. Assuming that the temperature is in equilibrium across the different components, the energy balance equation reads:

$$\frac{\partial S_T}{\partial t} + L\frac{\partial}{\partial t}\left[\rho_v n\left(1-S_r\right)\right] + \mathrm{div}\left(\mathbf{f}_T\right) + L\frac{\partial}{\partial t}\left(\mathbf{i}_v + \rho_v \mathbf{f}_g\right) - Q_T = 0 \tag{4}$$

where L is the latent heat of water vaporisation, $\mathbf{f}_T$ is the thermal flux, Q_T refers to the heat source and S_T is the enthalpy of the system, given by:

$$S_T = \left[\left(1-n\right)\rho_s c_{p,s} + nS_r\rho_w c_{p,w} + n\left(1-S_r\right)\left(\rho_a c_{p,a} + \rho_v c_{p,v}\right)\right]\left(T - T_0\right) \tag{5}$$

where $c_{p,i}$ corresponds to the heat capacity of the species i. The equilibrium of the medium is established as:

$$\mathrm{div}\left(\boldsymbol{\sigma}\right) + \mathbf{b} = 0 \tag{6}$$

where $\boldsymbol{\sigma}$ is the total stress tensor (considering compression positive) and $\mathbf{b} = \rho\mathbf{g}$ is the body force vector.

The equations above are implemented in the computer code LAGAMINE[27] integrated using finite elements in space and finite differences in time.

3.2 | Thermal and hydraulic constitutive laws

The following thermo-hydraulic (TH) constitutive relations are assigned to all materials in the simulation except for the steel canister.

The bulk density of liquid water is assumed to depend on p_w and T according to:

$$\rho_w = \rho_{w0}[1 + \chi_w(p_w - p_{w0}) - \beta_w(T - T_0)] \tag{7}$$

where $\rho_{w0} = 1\ \mathrm{Mg/m^3}$ is the bulk water reference density at a reference pressure $p_{w0} = 0.1$ MPa, and reference temperature $T_0 = 20\ ^\circ\mathrm{C}$, $\chi_w = 4.54 \times \cdot 10^{-10}\mathrm{Pa}^{-1}$ is the water compressibility and $\beta_w = 1.8^{-4}/^\circ\mathrm{C}$ is the water thermal expansion coefficient. The dynamic viscosity of bulk water μ_w evolves with T according to the empirical equation:

$$\mu_w = 0.6612(T - 229)^{-1.56} \tag{8}$$

where μ_w is expressed in Pa·s and T in Kelvin degrees.

Liquid flow is modelled by means of Darcy's law assuming an isotropic permeability tensor:

$$\mathrm{f}_l = -\frac{\mathbf{I}k_f k_{rw}}{\mu_w}\mathbf{grad}\left(p_w + g\rho_w \mathrm{y}\right) \tag{9}$$

where k_f is the water saturated intrinsic permeability, k_{rw} is the relative permeability and y is the vertical coordinate.

Gas pressure is kept constant (atmospheric pressure) in the simulations and vapor is assumed to flow according to Fick's law in porous medium:

$$\mathbf{i}_v = -n\left(1 - S_r\right)\tau D\rho_g \mathbf{grad}\left(\rho_v\right) \tag{10}$$

where $\mathbf{i_v}$ is the vapor flow, D is the diffusion coefficient and τ the tortuosity. The gradient of vapor density is computed as[34]:

$$\mathbf{grad}\ \left(\rho_v\right) = \frac{\rho_0 gRH}{RT}\mathbf{grad}\left(\frac{-s}{\rho_w g}\right) + \mathrm{RH}\left[\frac{\partial \rho_0}{\partial T} + \frac{\rho_0}{\rho_w RT^2}\right]\mathbf{grad}\left(T\right) \tag{11}$$

where ρ_0 is the saturated density of water vapor, $R = 8.314$ J/mol K, is the gas constant, RH is the relative humidity and $s = p_a - p_w$ stands for suction.

Heat transport is governed by both conduction and convection:

$$\mathbf{f}_T = -\Gamma\mathbf{grad}\left(T\right) + \left[c_{p,w}\rho_w \mathbf{f}_w + c_{p,a}\left(\mathbf{i}_a + \rho_a \mathbf{f}_g\right) + c_{p,v}\left(\mathbf{i}_v + \rho_v \mathbf{f}_g\right)\right]\left(T - T_0\right) \tag{12}$$

where Γ is the thermal conductivity of the mixture.

4 | FINITE ELEMENT MODEL

4.1 | Modelling setup

The model presented in this work is based on the FE experiment so that the early response of the buffer can be compared to experimental results. The finite element mesh of the buffer analysed is shown in Figure 2, which includes a concrete liner, bentonite pedestal, GBM backfill and canister. The model involves 2D plane-strain conditions, which are representative of a mid-section in the canister. The rock around the tunnel is assumed to be representative of the Opalinus Clay in the Mont-Terri rock laboratory where a marked bedding orientation with a dip of 34° towards the south-east.[30] As the focus of the study is on the bentonite buffer evolution, the boundaries of the model were defined at 100 m from the tunnel axis, which avoided undesired boundary effects.

The initial water pressure and temperature of the host-rock before the excavation takes place were set at 2.1 MPa and 18°C respectively, that is, representative of the FE tunnel in Mont Terri and homogeneous all throughout the Opalinus Clay domain. For the purposes of this study, the mechanical response of the Opalinus Clay was simplified and it was assumed that the liner is stiff enough that this does not impact the stress state inside the buffer. The stress state before the excavation was set isotropic at 5 MPa of effective stress. The excavation is simulated assuming that the liner is installed immediately. After excavation, a period of 2 years of ventilation is considered, that is, simulated by imposing a p_w on the liner surface consistent with the measured water content of 8% at the tunnel surface after ventilation.[30] Using the water retention relationship of Opalinus Clay measured by Ferrari et al.[37] the pressure is set to $p_w = -30$ MPa.

After the ventilation period the buffer and canister are emplaced all simultaneously and the heating sequence, controlled by power in the canister, is applied. The heating power evolution (Figure 3) is representative of the average expected for a MOX/UO2 canister.[38] To account for the spacing between canisters in 2D conditions the power was scaled down to 75%.[24] The GBM is emplaced with a $w = 5\%$ that corresponds to a RH = 33% while the bentonite blocks are emplaced at a higher water content of $w = 18\%$, corresponding to a RH = 80%. A specific gravity value of $G_s = 2.74$[39] is considered in order to compute the void ratio, e from the dry density. In the base case (Figure 2B) a homogeneous initial dry density of the GBM is set at 1.5 Mg/m^3, corresponding to an $e = 0.83$, that is, assuming that during emplacement a Fuller-type distribution is achieved without significant segregation.[39] The initial dry density of the bentonite pedestal is set to 1.69 Mg/m^3

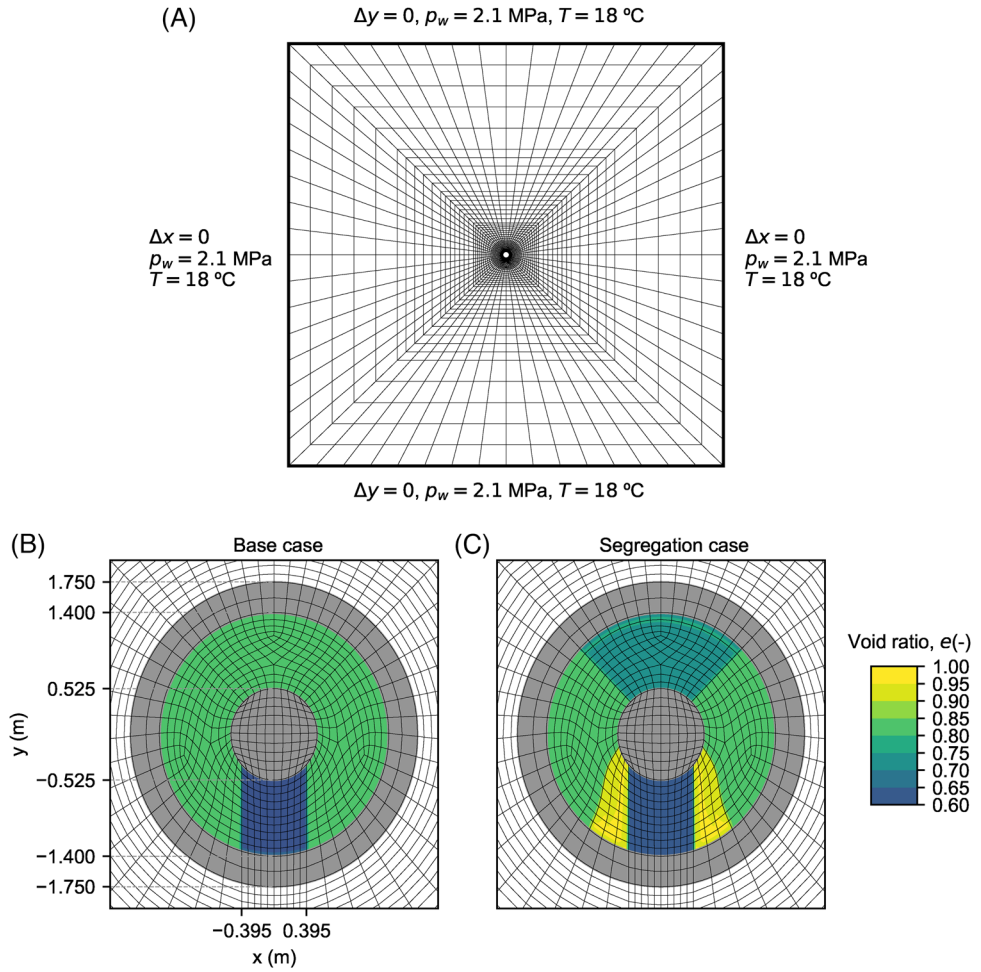

FIGURE 2 (A) Finite element mesh of the buffer analysed including boundary conditions in the outer zone. (B) Detailed view of the buffer mesh, with the initial distribution of void ratio for the Base case. (C) Distribution of the case simulating an initial segregation of the granular bentonite.

($e = 0.62$), that is, the average value including the technological gaps between blocks.[30] The simulation is performed up to 100,000 years representing the time for the canister to dissipate most of its radioactivity.

The initial distribution of e in the segregation case (Figure 2C) is based on the estimated profiles of dry density from the Emplacement test.[7,29] Above the canister, a higher dry density of 1.54 Mg/m^3 ($e = 0.78$) results from the configuration of the backfilling machine, whereas a lower density of 1.39 Mg/m^3 ($e = 0.98$) is considered around the pedestal. The remaining area is supposed to be filled with a dry density of 1.5 Mg/m^3 ($e = 0.83$).

4.2 | Constitutive relations and material parameters for the buffer

In order to account for the implications of the different initial dry densities of the bentonite, suitable constitutive relationships must be adopted. An essential feature of the analysis presented concerns the THM stress–strain constitutive model for the bentonite behaviour, which is based on the HM model presented in Bosch et al.[26] extended to thermo-elastoplasticity following the procedure proposed by Laloui and François.[40] The constitutive framework is outlined in the following, while the model equations are included in Appendix A. The model is formulated in the framework of a generalised effective stress, $\boldsymbol{\sigma}' = \boldsymbol{\sigma} - [p_a - (p_a - p_w)S_r]\mathbf{I}$, that is, linked to the mechanical elastic strains,[41] and S_r, and T, which express the variation of elastoplastic compressibility under unsaturated conditions[42] and the current yield pressure respectively. As a result, the elastic domain depends on the stress history, the current temperature and the degree of

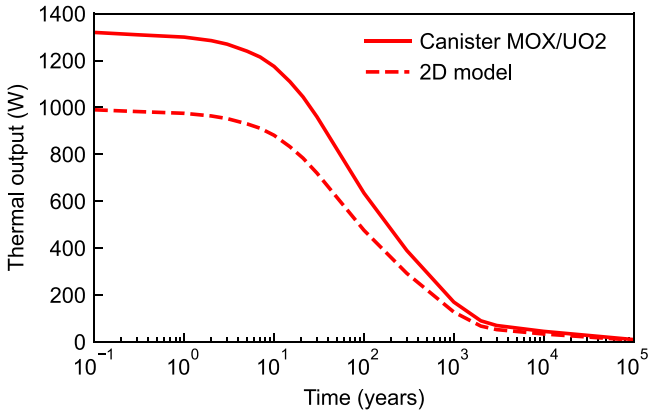

FIGURE 3 Heating power emitted by the MOX/UO2 canister and equivalent power for the 2D plane strain model.

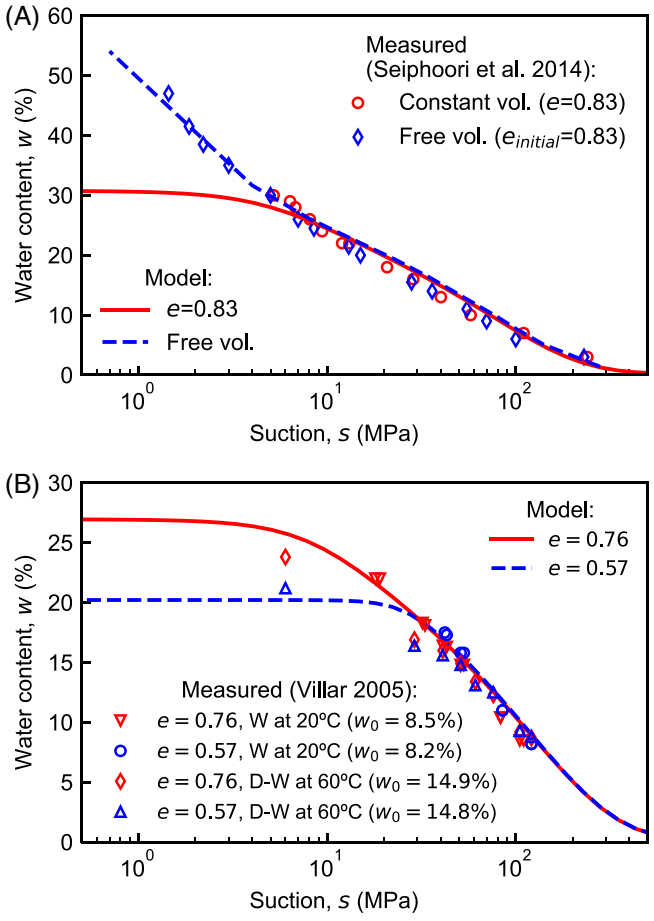

FIGURE 4 (A) Water retention calibration of granular bentonite (GBM) with data reported by Seiphoori et al.[39] under constant volume and free volume conditions. (B) Water retention of block bentonite calibrated with data obtained by Villar[43] for different wetting (W) and drying (D) paths at 20 and 60°C.

saturation. A water retention model that takes explicitly into account the existence of adsorbed water is used to predict the evolution of the degree of saturation with suction and deformation[4547].

Figure 4 shows the fit of the water retention model to experimental data. The water retention of the GBM was calibrated with data reported by Seiphoori et al.,[39] which involved GBM at an initial void ratio of $e = 0.83$, hydrated under free volume conditions and constant volume conditions (Figure 4A). The division of water content into adsorbed water and free water enables to reproduce both constant volume hydration and free swelling hydration. At high suctions most water

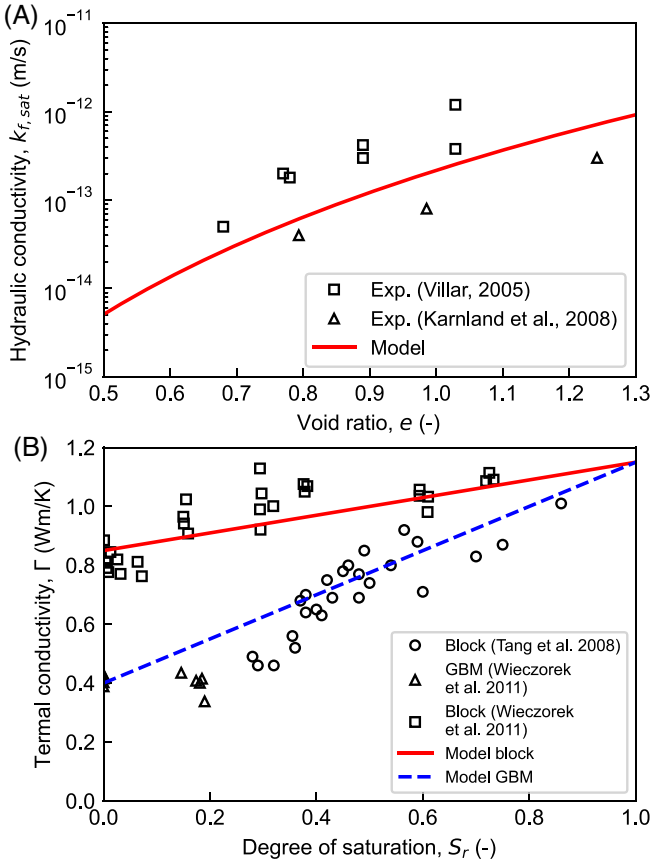

FIGURE 5 (A) Calibration of the saturated hydraulic conductivity as a function of void ratio with experimental data (Exp.) from Villar[43] and Karnland et al.[10] (B) Calibration of the thermal conductivity as a function of the degree of saturation with experimental data from Tang et al.[46] and Wieczorek et al.[44]

is expected to be in adsorbed form and therefore independent on the void ratio,[45] whereas at low suctions the water held by capillarity and diffuse double layer is modelled as a dependency on the void ratio.[47] The experimental data on compacted MX80 bentonite reported by Villar[43] was used to calibrate the water retention for the block pedestal, which consisted on hydration under constant volume conditions at different temperatures and void ratios. On that material, Villar[43] did not observe significant hysteresis upon wetting after drying (Figure 4B), which is the most representative path to which bentonite is subjected in the buffer, therefore no hysteresis in the water retention is considered in the analysis. No temperature dependency is included in the water retention curve, in accordance with the data from MX80 block bentonite at 60°C, as it does not indicate significant differences with the bentonite tested at 20°C (Figure 4B).

The hydraulic conductivity was calibrated with data reported by Villar[43] and Karnland et al.[10] obtained at ambient temperature ($T \cong 20$ °C) in a range of void ratio between 0.6 and 1.1 as shown in Figure 5A, where $k_{f,sat} = g\rho_{w0}k_f/\mu_w$ with $\mu_w = 10^{-3}$ Pa·s. The dependency of k_f on void ratio was taken into account by means of a modified Kozeny–Karman formula:

$$k_f = k_{f,0}\,\frac{(1-n_0)^{MKC}}{n_0^{NKC}}\,\frac{n^{NKC}}{(1-n)^{MKC}} \tag{13}$$

where $k_{f,0}$ is the initial intrinsic permeability for a porosity n_0 and MKC and NKC are material parameters. In the absence of additional experimental data, it was assumed that in saturated states there are no differences between the k_f of the GBM and the pedestal.

The thermal conductivity of the bentonite as a function of the degree of saturation was derived from data shown in Figure 5B reported by Wieczorek et al.[44] on GBM and blocks and Tang et al.[46] on compacted MX80 at different void ratios.

TABLE 1 List of intrinsic material parameters for the MX80 bentonite.

Parameter	MX-80
κ	0.068
ν	0.35
λ_s	0.112
$p'_{NCL}(e = 1,\ S_r = 1, T = T_r\ )$	2.2 MPa
ϕ'	11°
α	0.38
$p_r^{'}$	1 Pa
a	0.9 MPa^{-1}
b	1.5
n	1.8
e_{ads}	0.55
γ_T	0.15
β_{T0}	1.5×10^{-5}
$k_{f,0}(\ e_0 = 0.85)$	10^{-20} m^2
MKC	6
NKC	5
τ	0.8

The following expression was used to fit the data:

$$\Gamma\ = \Gamma_0\ + \Gamma_1 S_r \tag{14}$$

Once the TH properties were defined for the bentonite materials, the mechanical behaviour was calibrated. One of the main assumptions is that the parameters defining the saturated state behaviour of both GBM and block are coincident and that, at isothermal saturated state, the position of the normal compression line (NCL) does not depend on the initial state nor on the stress history of the material.[4,26,28] The same parameters calibrated and reported in Bosch et al.[26] for the MX80 at saturated states were used in this study (Table 1). Swelling pressure tests in mixtures of pellets and powder were used to determine the loading collapse curve parameters of the GBM. In addition, a swelling pressure test in which bentonite was emplaced at two different dry densities is considered. The same tests are used in order to back-analyse k_{rw} using an exponential dependency on S_r:

$$k_{rw} = S_r^{\alpha_k} \tag{15}$$

where α_k is a material parameter.

Figure 6 shows the calibration of the granular bentonite against the pellets and powder mixture that had an average dry density of 1.49 Mg/m^3. This test is further discussed in Bosch et al.[26] and the same calibration was used in this study. The nonlinear development of swelling pressure, which captures well the experimental measurements, results from the coupling between the water retention behaviour and the generalised effective stress framework, involving the Bishop-type stress and the dependency of plastic compressibility on S_r. Figure 7 shows the swelling pressure test presented by Bernachy-Barbe[13] where two compacted blocks at densities of 1.4 and 1.56 Mg/m^3 were placed in the same oedometer ring. This test is of interest because these densities are close to the upper and lower bounds of dry density that was measured in the backfill emplacement test.[7] The lower density block was placed at the bottom, from where hydration took place by means of constant water pressure. Although the average void ratio and height are very similar to the previous test, and thus the swelling pressure, the significant difference in time required to reach equilibrium indicates that it is not straightforward to analyse the problem with a single equivalent void ratio and hydromechanical properties.

The bentonite block pedestal is assumed to behave as MX80 bentonite. Its behaviour upon wetting was calibrated as shown in Figure 8 with a swelling pressure test reported by Pusch[48] on a sample with a height of 21 mm and a void ratio of around 0.63, that is, representative of the overall void ratio of the pedestal including gaps between the blocks. Only the parameters $\zeta, \xi,\ r,\ m$ and α_{kw} differ from the GBM (Table 2).

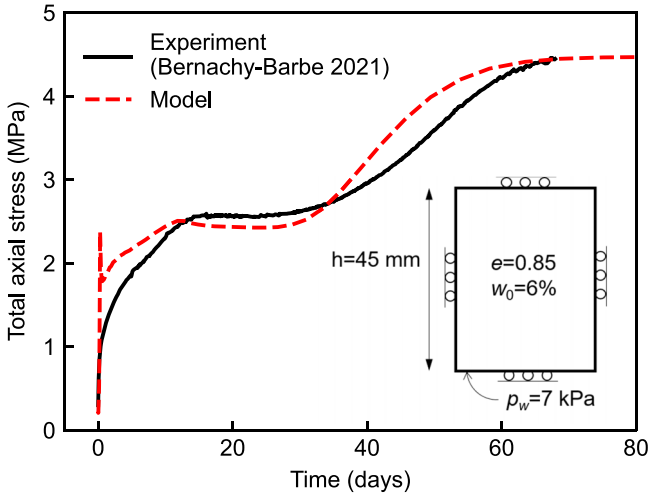

FIGURE 6 Calibration of the behaviour of granular bentonite with an initial void ratio $e = 0.85$ subjected to hydration under constant volume at isothermal conditions (after Bosch et al.,[26] with experimental data reported by Bernachy-Barbe[13]).

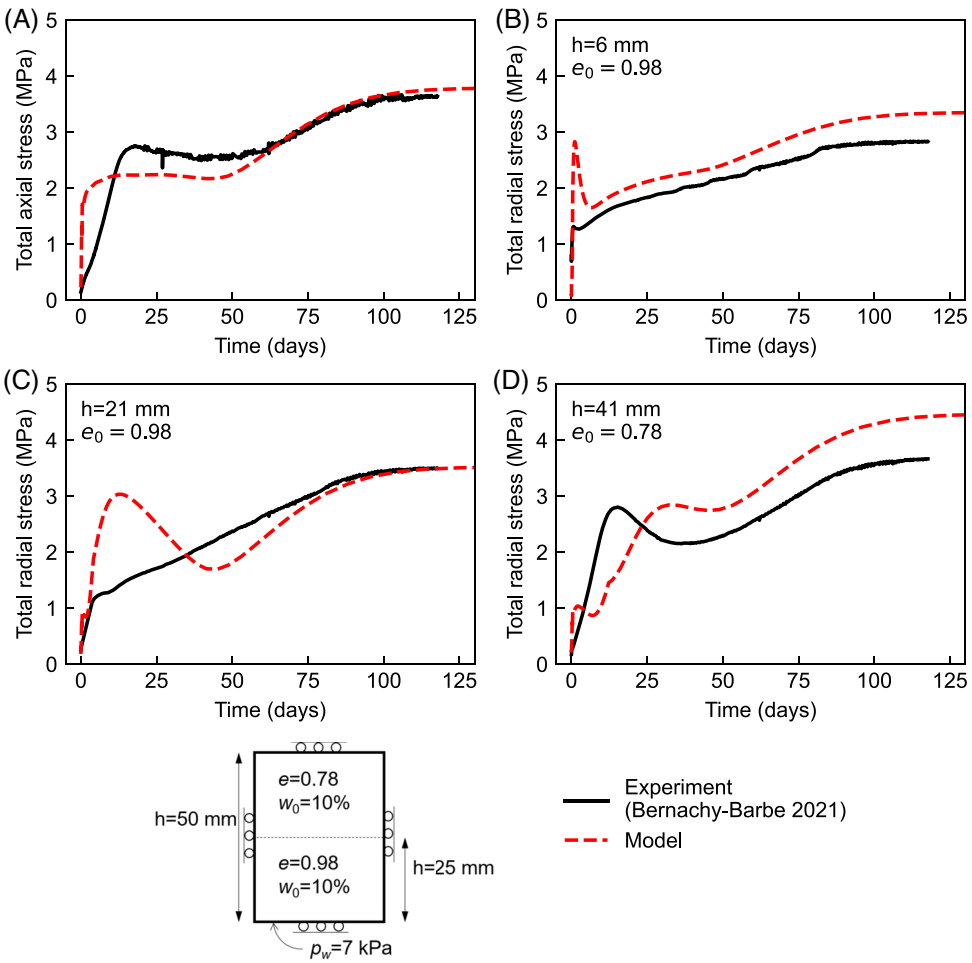

FIGURE 7 Calibration of the behaviour of bentonite with an initial void ratio $e = 0.78$ and $e = 0.98$ subjected to hydration from the side at $e = 0.98$ under overall constant volume at isothermal conditions. Experimental data reported by Bernachy Barbe.[13] (A) Axial stress. (B) Radial stress at 6 mm from the water uptake. (C) Radial stress at 21 mm from the water uptake. (D) Radial stress at 41 mm from the water uptake.

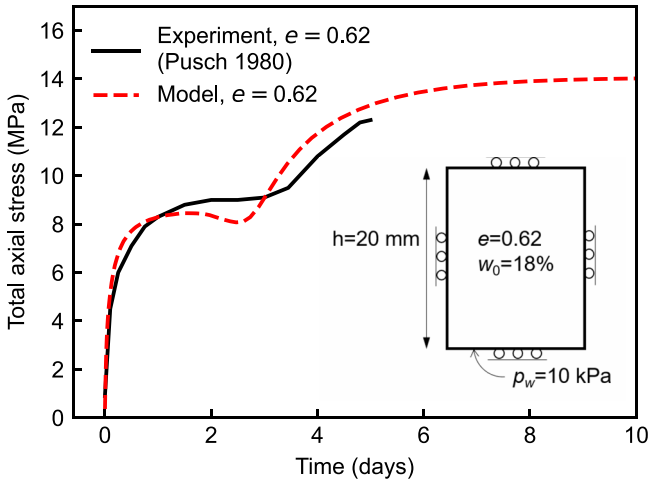

FIGURE 8 Calibration of the behaviour of the bentonite pedestal with an initial void ratio $e = 0.62$ subjected to hydration under constant volume at isothermal conditions. Experimental data reported by Pusch on MX80 bentonite (1980).

TABLE 2 List of parameters used for the pellets/powder mixture and the block bentonite

Parameter	GBM ($e_0 = 0.98$)	GBM ($e_0 = 0.83$)	GBM ($e_0 = 0.78$)	Block ($e_0 = 0.62$)
Γ_0, Γ_1 (Wm/°K)	0.4, 0.75	0.4, 0.75	0.4, 0.75	0.85, 0.3
r	0.35	0.29	0.23	0.22
ζ	2.7	2.1	2.7	2.5
ξ	0.9	0.9	0.8	0.5
α_{kw}	4	4	4	2.9
m	0.65	0.65	0.65	1.0

TABLE 3 List of material parameters for the host rock (Opalinus clay) and concrete liner

Parameter	Host rock	Concrete
$\mathbf{k}_f$ (m^2)	$k_{f\,par} = 5 \times 10^{-20}$ $k_{f\,per} = 1 \times 10^{-20}$	$k_f = 1.7 \times 10^{-17}$
$\mathbf{\Gamma}$ (Wm/°K)	$\Gamma_{par} = 2.1$ $\Gamma_{per} = 1.2$	$\Gamma = 2$
α_{VG}(MPa)	30	1
λ_{VG}	1.8	1.25
E (GPa)	7	30
ν	0.27	0.20
Initial porosity n	0.183	0.23

Some studies have reported a decrease in swelling pressure of bentonites as a result of a temperature increase[49] which is a response that the thermo-plastic formulation allows to take into account through the thermal collapse curve.[40] For both GBM and pedestal blocks, a thermal plasticity parameter of $\gamma_T = 0.15$ was used, which implies a decrease of swelling pressure of 20% from 20 to 70 °C according to data presented by Pusch et al.[50] All intrinsic material parameters for the bentonite are reported in Table 1, while Table 2 summarises the parameters that depend on its initial state.

4.3 | Constitutive relations and parameters for the canister, liner and host-rock

The main THM parameters for the host rock and the concrete liner are summarised in Table 3. Mechanical interactions between the buffer and the tunnel support and the host rock are beyond the scope of this study and therefore their mechanical response is assumed to be isotropic linear elastic. The thermal and hydraulic parameters for the host rock are

representative of the Opalinus Clay in the Mont-Terri rock laboratory.[51–53] As in the FE experiment the principal directions of thermal conductivity and hydraulic conductivity were considered to be rotated 33° with respect to the tunnel horizontal axis.[54] A van-Genuchten form of water retention curve and relative water permeability[55] was adopted for the Opalinus Clay:

$$S_r = \left[1 + \left(\frac{s}{\alpha_{VG}}\right)^{\lambda_{VG}}\right]^{\frac{1}{\lambda_{VG}}-1} \tag{16}$$

$$k_{rw} = \sqrt{S_r}\left[1 - \left(1 - S_r^{\frac{1}{\lambda_{VG}}}\right)^{\lambda_{VG}}\right]^2 \tag{17}$$

where α_{VG} and λ_{VG} are material parameters that were calibrated with data from Ferrari et al.[37] The same constitutive equations are used for the concrete lining and its parameters have been either derived from Muller et al.[30] or assumed as representative values. Properties representative of steel are assigned to the canister, characterised by a thermo-elastic law with $E = 210$ GPa, $\nu = 0.25$ and a volumetric thermal expansion coefficient of $4 \times 10^{-4}\,°\mathrm{C}^{-1}$.

5 | BASE CASE RESULTS

5.1 | Comparison between the FE results and the model

In this section model results are compared to the temperature, relative humidity and heater displacement measurements that are available from the operation of the FE experiment. The objective of the comparison is to support the model assumptions by verifying that the trend and order of magnitude of the processes are captured.

Temperature and RH measurements from a section corresponding to the heater #3, close to the heater surface are shown in Figure 9 together with the model predictions. The evolution of temperature is well captured by the model for both the GBM and the pedestal. In terms of relative humidity, the model predicts a strong drying of the bentonite blocks in line with the experimental measurements from the initial state of RH = 80%, to values that are close to the GBM. A small initial increase in RH was measured both in the pedestal and the GBM. The model captures this increase for the pedestal as a result of vapour transfer from the canister contact, but not for the GBM, which could be partially due to the initial exposure of the GBM with the initial RH in the tunnel gallery. Figure 10 shows the measurements of temperature and RH in two points close to the shotcrete and the respective model predictions. While the trend is also well captured some quantitative discrepancies are observed. Nevertheless, taking into account that the 3D nature of the problem has been simplified to plane strain conditions the modelling predictions are considered satisfactory.

Figure 11 shows the monitored heater position through LVDTs,[31] together with the model results, both of them revealing a settlement of the heater. This result is essentially linked to the strong drying of the bentonite blocks in the early stage and the stress paths that lead to this model prediction are discussed afterwards. The difference between the top and bottom displacements is due to the dilation of the steel and is in qualitative agreement with the experimental measurements.

5.2 | Long-term prediction of temperature, saturation and swelling pressure

The predicted temperature evolution in the long term is shown in Figure 12. The maximum temperature at the canister surface, around 120°C, is reached after 7 years. The heat dissipates faster through the bentonite pedestal as a consequence of the higher water content and initial S_r that involves a higher conductivity on average. Conversely, in the cooling phases the GBM and the pedestal show similar rates of temperature decrease mostly due to the saturated state that leads to a more homogeneous thermal conductivity. The sudden changes in temperature during the cooling phase are related to the discrete steps of the power output sequence.

The evolution of the degree of saturation is shown in Figure 13 for the same points. The block pedestal is subjected to a substantial drying close to the canister, as noted also from the measurements of RH. Initially emplaced at $S_r = 0.8$, they are subjected to drying up to values lower than $S_r = 0.2$. This drying is limited to the first few years, before the

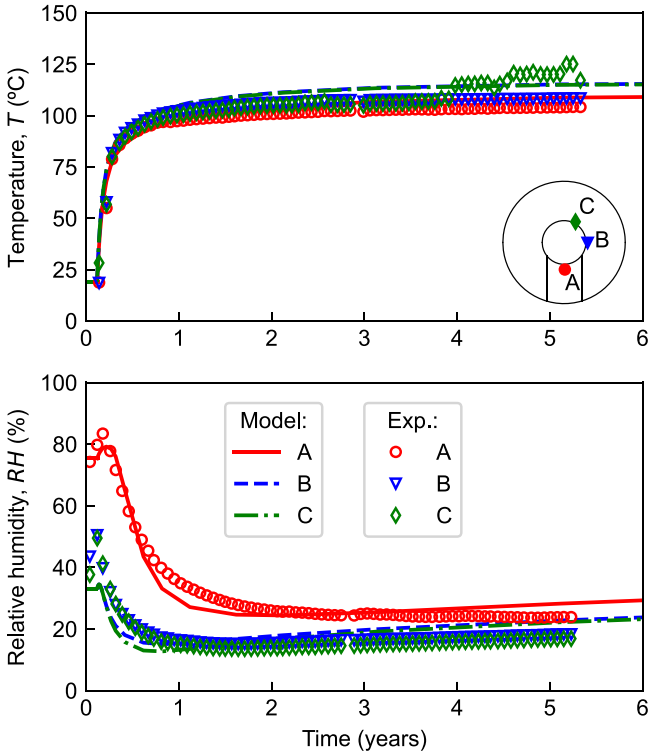

FIGURE 9 Experimental results from the FE experiment[31] at monitoring points close to a heater (denoted by Exp.) and corresponding model results.

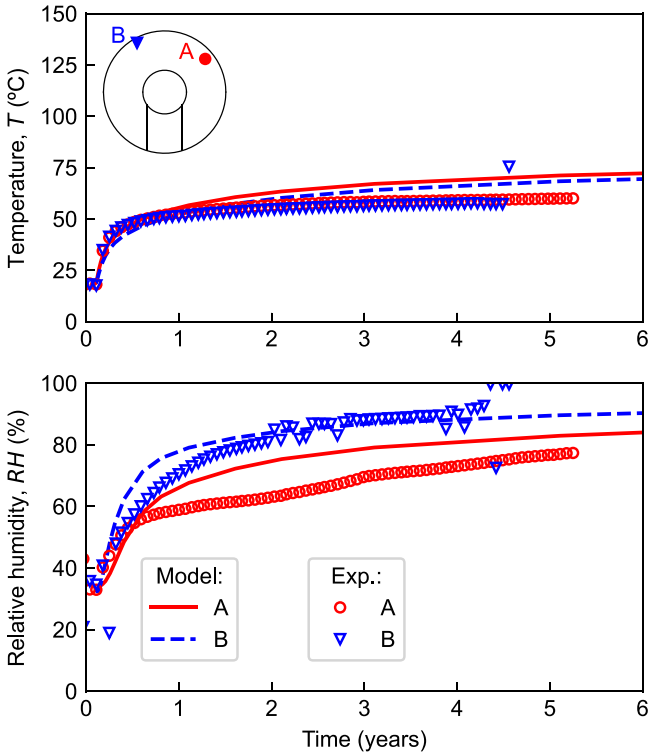

FIGURE 10 Experimental results from the FE experiment[31] at monitoring points close to the concrete support (denoted by Exp.) and corresponding model results.

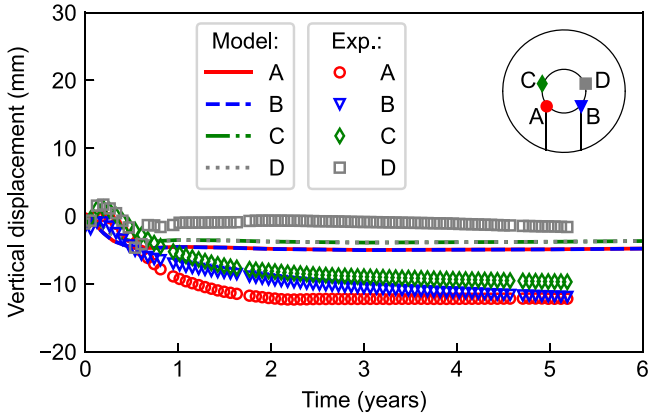

FIGURE 11 Measured displacements of one of the heaters in the FE experiment[31] and model results of the upper and lower part of the canister.

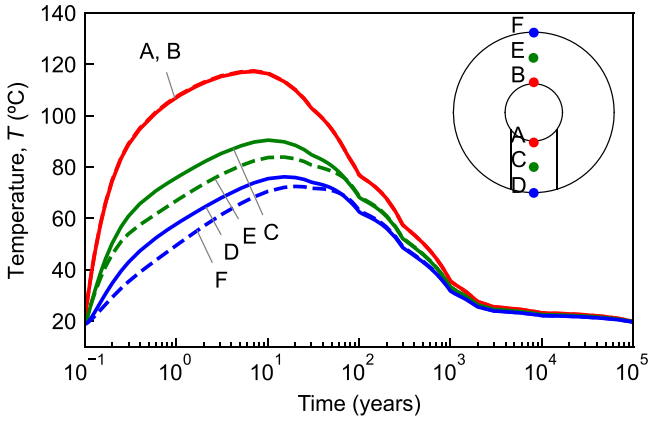

FIGURE 12 Long-term prediction of the temperature evolution at six points of the buffer.

temperature peak is reached and afterwards the buffer is globally hydrated. Although S_r quickly increases at external points of the buffer for the first years, the saturation rate tends to decrease substantially, and full saturation is reached at fairly the same time all throughout the barrier. This is a result of the coupled hydro-mechanical behaviour; while the external bentonite hydrates, the void ratio increases and therefore the S_r tends to evolve slower. The opposite occurs at internal points, where S_r increases not only due to hydration but also due to compression from the external bentonite. The complete saturation of the buffer is predicted to be achieved after 80 years of operation.

The development of swelling pressure, expressed as the normal pressure close to the canister and the tunnel liner, is shown in Figure 14. The saturation phase is characterised by a non-monotonic development of stresses, including a period in which the total pressure of the block pedestal is lower than the pressure developed by the GBM as a result of the initially strong drying, which starts to compensate by hydration after around 5 years of operation (Figure 14A). Around the liner (Figure 14B), the swelling pressure is observed to be practically the same at points C and D, which indicates that the anisotropic thermal and hydraulic conductivity of the host rock do not play a relevant role in its development. This was further verified by comparing the hydration in the points aligned with the principal directions of anisotropy, which showed negligible differences.

Once full saturation is attained a significant stress build-up develops. This is linked to the thermal pressurisation of pore water as a consequence of the very low permeability of the geological and engineered barriers, and it has been described in a previous TH study by Senger et al.[56] The water pressure build-up is depicted in Figure 15, along with the initial value (before excavation) where it can be observed that once saturated, pore pressure evolves simultaneously throughout the buffer. The pressure in excess of the initial state is predicted to be around 3.5 MPa and it is dissipated after 1000 years, as the initial field of temperature is recovered towards a steady state.

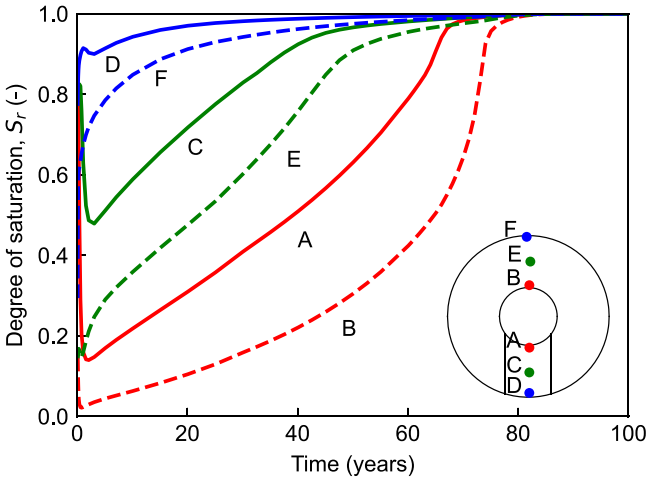

FIGURE 13 Predicted evolution of the degree of saturation in the buffer.

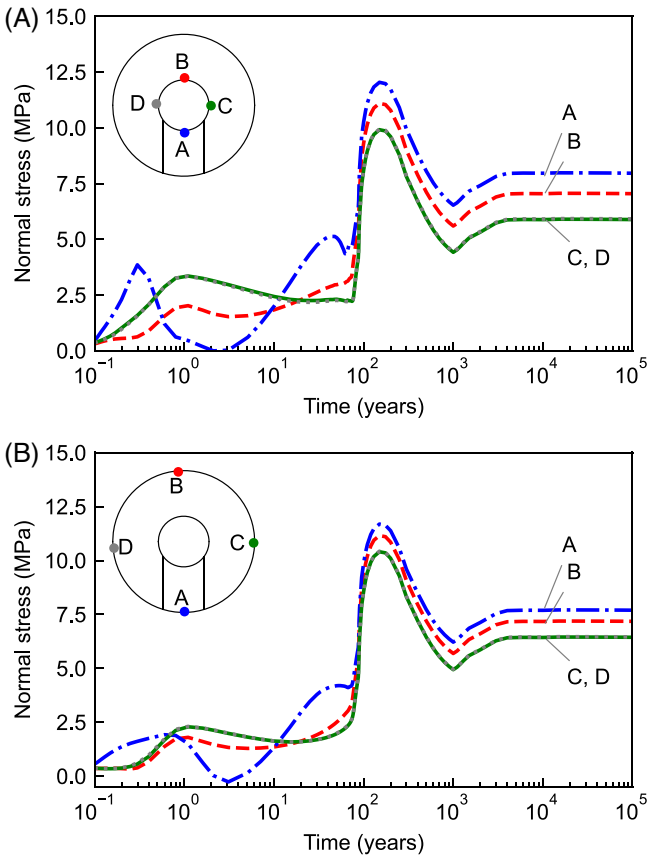

FIGURE 14 Predicted developement of total stress (swelling pressure) in the buffer. (A) Normal stress acting on the canister. (B) Normal stress acting on the concrete liner.

It can be seen that at steady state, the difference in swelling pressure between the block zone and the GBM is not as significant as the laboratory tests on the materials alone would suggest, being instead an intermediate value. This can be better observed in Figure 16, which shows the mean swelling pressure and final dry density predicted by the model in each element of the buffer, divided into two categories: elements belonging to the pedestal and to the GBM. Indeed, contrary to the constant volume tests, bentonite blocks have the capacity to swell and the GBM is compressed by the blocks. The final dry density in the buffer varies from 1.5 to 1.6 Mg/m^3 and the swelling pressure developed ranges from 4.2 to 8.0 MPa, which is between the range of swelling pressure measurements reported for MX80 bentonite.

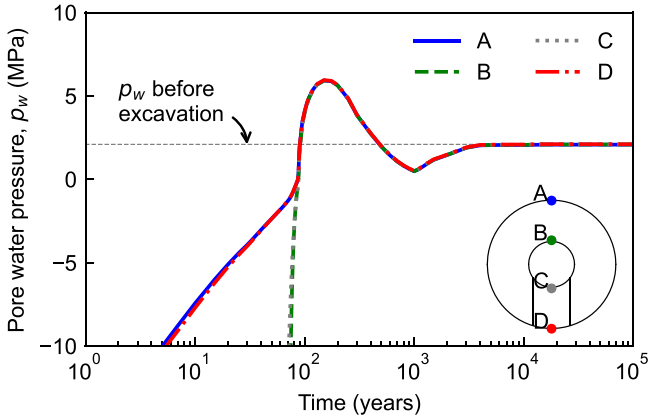

FIGURE 15 Predicted development of pore water pressure in the long term.

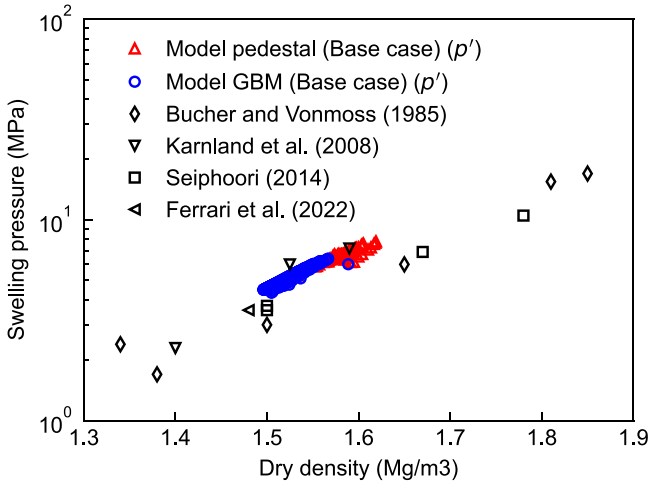

FIGURE 16 Local dry density-swelling pressure (in terms of mean effective stress) predicted in the buffer (Base case) at steady state compared to experimental swelling pressure test results from literature (Refs. 9, 10, 28, 57).

5.3 | Evolution of dry density and canister displacement

Figure 17 shows the spatial evolution of the void ratio and the degree of saturation at four times during the saturation phase, allowing the visualisation of the interaction between the pedestal and GBM as well as their trend to homogenise. The heterogeneity of the initial state is characterised by $S_r = 0.8$ and $e = 0.62$ in the pedestal, as opposed to $S_r = 0.2$ and $e = 0.83$ in the GBM. After 40 years of operation (Figure 17B) no significant differences are observed in terms of void ratio, except for some asymmetric hydration from the host rock. In contrast the spatial variability of S_r is significant, mostly induced by the thermal and hydraulic gradients. The low variability in void ratio at this stage is related to the high stiffness and low swelling pressures of the bentonite at high suctions. As the saturation of the buffer proceeds (Figure 17C), it is observed that the interface between the pedestal and GBM starts to converge in terms of void ratio, as a result of the swelling of the block, and the increased compressibility of the saturated GBM. Once the internal zones of the buffer become saturated, they swell and tend to compress the outer zones, although the initial state is not recovered as a result of the stress-path dependency of bentonite behaviour. Consequently, a rather homogeneous state is achieved at saturation in comparison to the initial state (Figure 17D).

The non-uniform swelling and compression upon heating, drying and hydration result in movements of the canister as already described. Figure 18 shows the displacement of the canister over the course of time. It is observed that the initial movement downwards is restricted to the first years, and that a change in trajectory develops as hydration proceeds and temperatures decrease. The overall higher swelling strains developed by the pedestal implies that the canister moves

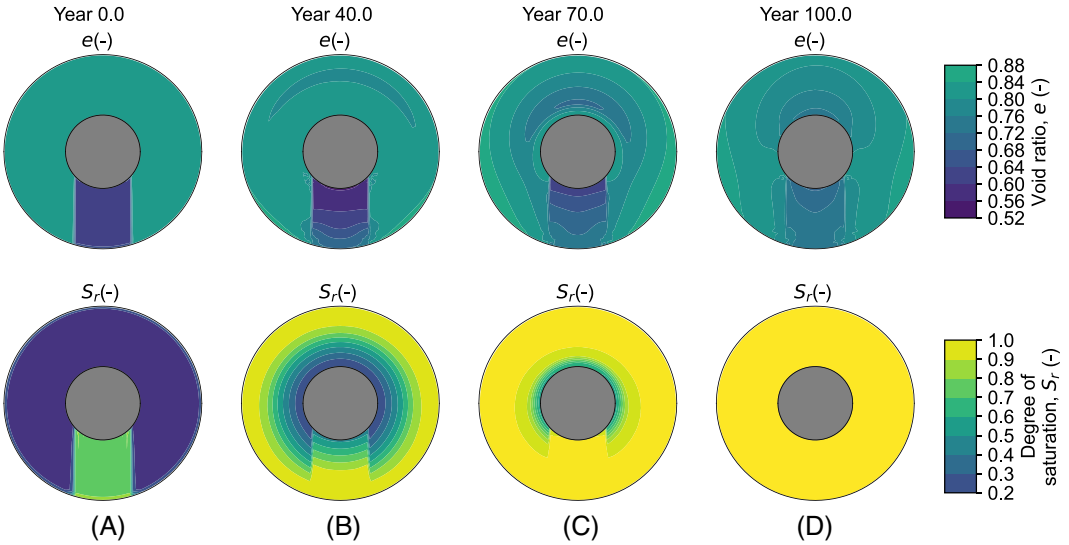

FIGURE 17 Predicted evolution of the spatial distribution of the void ratio and degree of saturation (Base case). (A) Initial state. (B) After 40 years. (C) After 70 years. (D) After 100 years.

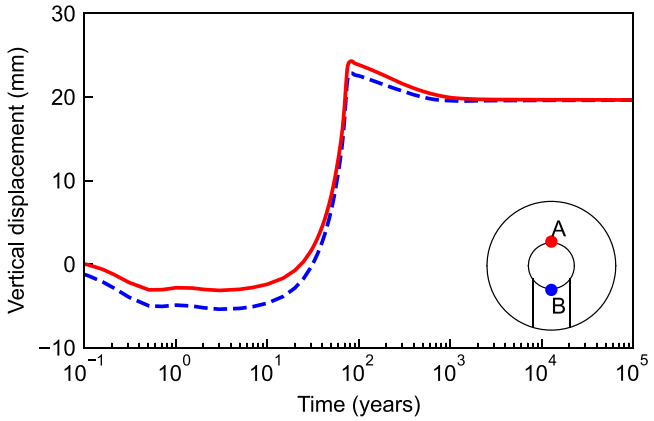

FIGURE 18 Long-term displacement of two points corresponding to the top and lower sides of the canister.

upwards and reaches a steady state position 20 mm higher from its initial position. It can be noted as well that the pore water pressure build-up at saturation (Figure 15) does not significantly affect the position of the canister.

In order to better understand the sources of the displacement, the stress path to which the pedestal is subjected at two points are represented in Figure 19 in terms of the constitutive variables of the stress–strain model (p', S_r, e, T). It can be identified the decrease in S_r close to the canister, that is, induced by the elevated temperatures, which results in an increase of p' trough an increase in sS_r. Although the external point tends to swell as a result of hydration, the increase in p' of the inner point results in an overall shrinkage of the pedestal. Once the peak temperature is reached, after about 10 years of operation, S_r of the inner point increases due to both temperature decrease and suction decrease, resulting in swelling for both points and a heave of the canister. As it can be observed, the void ratio is close to equilibrium after about 100 years and does not change significantly throughout the cooling process, suggesting that most mechanical changes are expected to occur during the saturation stage.

5.4 | Effects of segregation upon emplacement

The effects of an initial non uniform distribution of GBM dry density are compared to the base case in terms of saturation rate, swelling pressure on the canister, spatial evolution of void ratio and canister displacement.

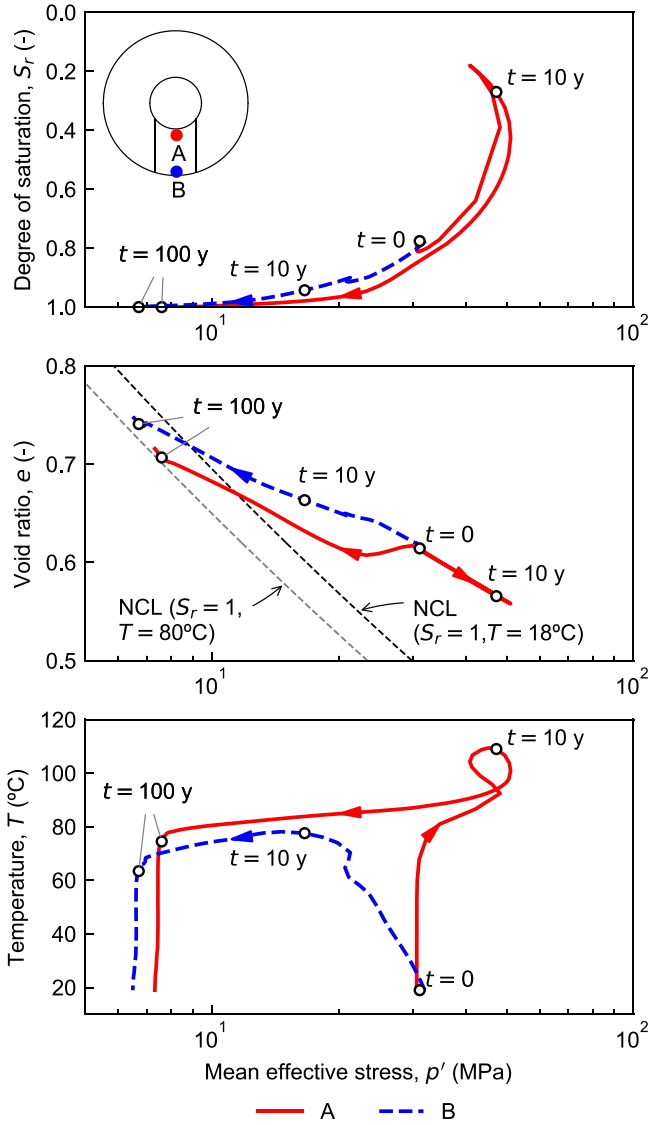

FIGURE 19 Generalised stress paths in terms of (p',S_r,e,T) of two points in the bentonite block pedestal.

Figure 20 shows the evolution of S_r and total normal stress in three points close to the canister for both the base case and the segregation case. The buffer becomes saturated around 5 years earlier in the case of segregated GBM, without significant differences in the rate of saturation of the pedestal. While the intrinsic permeability is lower for higher dry density, the lower void ratio implies a higher air entry value and saturation is reached faster as a result of a higher relative permeability for a given suction. This result indicates again the importance of considering a water retention model coupled to the mechanical state, in this case through the current dry density of the bentonite.

A comparison of the swelling pressure development between the base case and the segregation case can be made in Figure 20. As a consequence of the higher dry density on the top part, the swelling pressure increases about 1 MPa. The swelling pressure on the lower part is not affected by the different distribution of dry density. Conversely, the lateral pressure during the saturation phase is slightly lower in the segregation case despite that the initial dry density is the same at this area in both cases, although this difference reduces as full saturation is approached.

The spatial distribution of the void ratio and the degree of saturation at t = 10, 40, 70 and 100 years is shown in Figure 21. The initial distribution is not significantly modified until S_r approaches 1 locally, and once saturated, the void ratio distribution tends to homogenise. Comparing it with the base case (Figure 17) it appears that GBM segregation, at least in the studied configuration, does not significantly impact the void ratio distribution after saturation and therefore does not degrade the buffer performance from a mechanics point of view. A more quantitative comparison between the two cases can be done based on Figure 22 which shows the profiles of dry density in the vertical section centered with the canister.

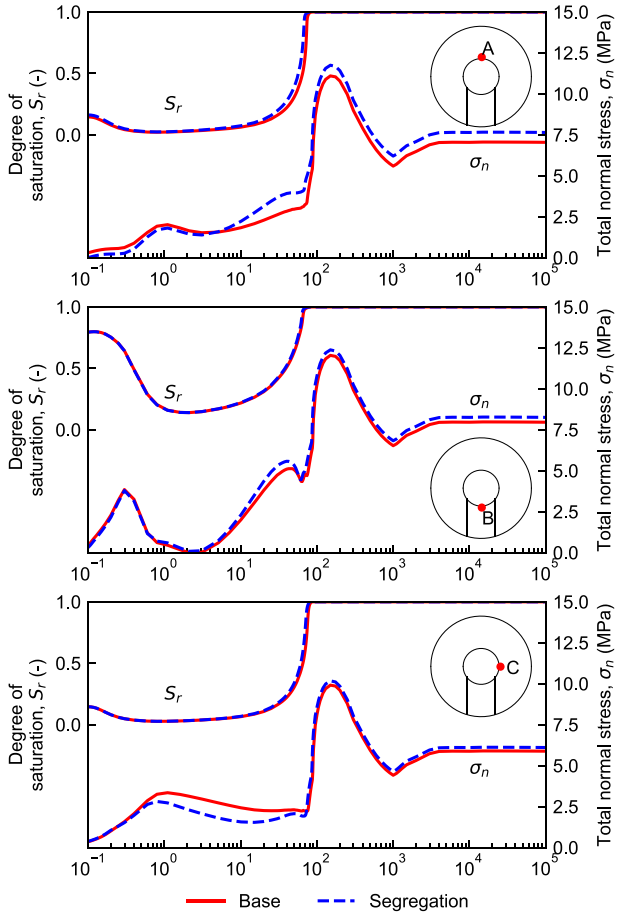

FIGURE 20 Evolution of the normal stress on the canister in the base case and in the segregated granular bentonite case at three points.

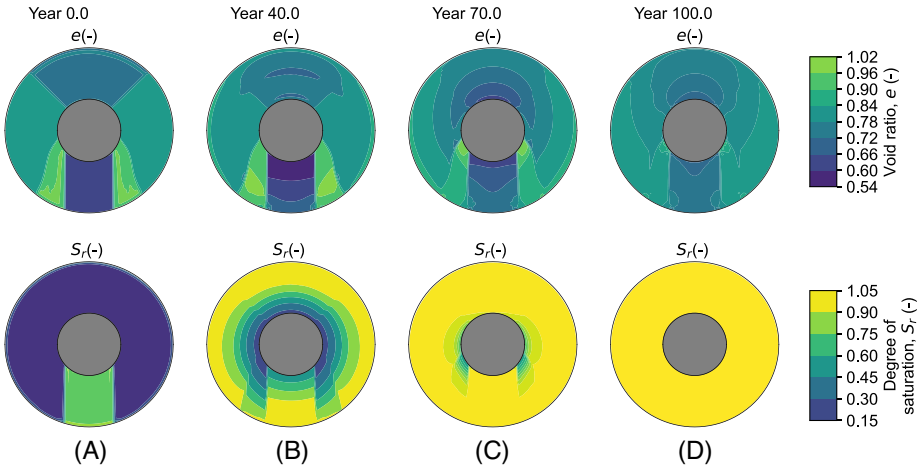

FIGURE 21 Evolution of the spatial distribution of the void ratio and degree of saturation in the initially segregated buffer case. (A) Initial state. (B) After 40 years. (C) After 70 years. (D) After 100 years.

While the profile in the GBM displays similar shape between the two cases, but with higher density for the segregated case, the difference in density after saturation is around three times lower than after emplacement, indicating the tendency of bentonite to homogenise upon saturation. However, negligible differences exist between the final profiles in the middle of the pedestal.

The displacement of the canister in both the base and the segregation cases can be compared in Figure 23. While at early stage the displacement is quite similar, after saturation it is observed that in the segregation case the upwards displacement

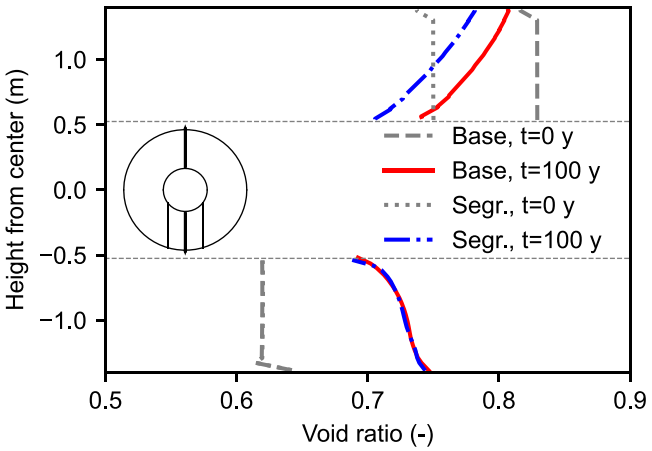

FIGURE 22 Initial profiles and profiles after saturation ($t = 100$ years) of dry density in the vertical section centred with the canister of the two cases.

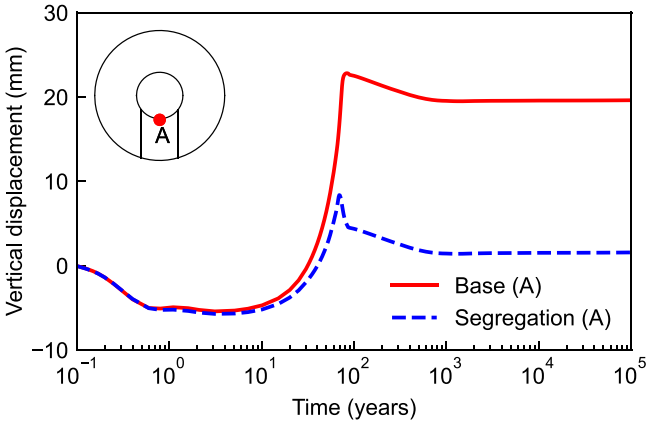

FIGURE 23 Canister displacement (point A) in the segregated granular backfill case as compared to the base case.

is significantly prevented. This is somehow an opposite result from the evolution of void ratio, that is, most differences with the base case arise after the saturation phase instead of during the saturation phase. It is explained by the fact that at early stage is the thermal process that affects the mechanical response of the pedestal through drying and shrinkage, while the GBM is practically unaffected due to its lower water content at emplacement. Once full saturation is approached, the swelling pressure starts to develop significantly and the higher swelling potential of the upper GBM, added to the lower swelling potential of the GBM close to the pedestal, prevents canister heave while enhancing homogenisation by compressing the GBM at lower density.

6 | CONCLUSIONS

This study analysed the THM performance of a clay buffer for nuclear waste disposal composed by bentonite blocks, that support the HLW canister, and a granular bentonite mixture (GBM), that allows for an efficient backfill. The mechanical response up to hydraulic steady state of this layout, that is, achieved after around 4000 years of its emplacement, has been numerically analysed using a fully coupled THM finite element formulation. Because of its importance, the stress–strain constitutive model for the bentonite, as well as the thermo-hydraulic constitutive parameters, have been calibrated using several experimental datasets from the literature.

Two initial distributions of the void ratio of the granular backfill have been analysed. The base case scenario supposes that the void ratio distribution of the granular pellet mixture is uniform, while the alternative case assumes a void ratio distribution affected by segregation during the emplacement. While the three-dimensional nature of the problem has been

simplified to two-dimensional plane strain conditions, comparison with experimental results of a large scale in situ test provided a satisfactory validation of the model hypothesis.

In spite of higher overall density, that implies lower saturated permeability, full saturation of the buffer is reached after 75 years in the GBM segregated case as compared to 80 years in the homogeneous GBM case. At the time of saturation, the temperature is between 60 and 80°C. Although there are significant differences between the swelling potential of the block pedestal and the GBM, the swelling pressure developed in the buffer is relatively homogeneous, with peak values of 12 MPa as a result of thermal pressurisation of water after saturation. Segregation of the GBM does not influence the final swelling pressure neither its spatial distribution. In both cases the model predicts a more homogeneous distribution of void ratio after saturation with respect to the initial state, with the upper and lower part of the canister presenting higher density.

Although in both cases the canister moves downwards in the early stage as a result of the drying induced shrinkage of the pedestal, after 10 years the hydration and swelling of the pedestal blocks starts to compensate this settlement. At full saturation, the canister equilibrates about 20 mm above its initial position in the homogeneous GBM case while it remains close to the initial position in the segregated GBM case.

ACKNOWLEDGEMENTS

This work has received funding from the Euratom research and training programme 2014−2018 under grant agreement No 745942. Open access funding provided by Ecole Polytechnique Federale de Lausanne.

DATA AVAILABILITY STATEMENT

The data that support the findings of this study are available from the corresponding author upon reasonable request.

ORCID


Jose A. Bosch https://orcid.org/0000-0003-0608-7883

REFERENCES

1. Sellin P, Leupin OX. The use of clay as an engineered barrier in radioactive-waste management–a review. *Clays Clay Miner*. 2013;61(6):477-498.
2. Börgesson, L., Johannesson, L. E., Sanden, T., & Hernelind, J. Modelling of the physical behaviour of water saturated clay barriers. Laboratory tests, material models and finite element application (No. SKB-TR–95-20). Swedish Nuclear Fuel and Waste Management Co. 1995.
3. SKB. Environmental impact statement. Interim Storage, Encapsulation and Final Disposal of Spent Nuclear Fuel; 2011.
4. Middelhoff M, Cuisinier O, Masrouri F, Talandier J. Hydro-mechanical path dependency of claystone/bentonite mixture samples characterized by different initial dry densities. *Acta Geotech*. 2021;16(10):3161-3176.
5. Zeng Z, Cui YJ, Zhang F, Conil N, Talandier J. Investigation of swelling pressure of bentonite/claystone mixture in the full range of bentonite fraction. *Appl Clay Sci*. 2019;178:105137.
6. NAGRA. *Project Opalinus Clay: safety report. Demonstration of disposal feasibility (Entsorgungsnachweis) for spent fuel, vitrified high-level waste and long-lived intermediate-level waste*. Technical Report NTB 02–05, NAGRA; 2002.
7. Köhler S, Garitte B, Weber HP, Müller HR. FE/LUCOEX: Emplacement Report. Nagra working report, NAB 15- 27, Nagra, Wettingen, Switzerland and EU Project LUCOEX, Deliverable D2.5; 2015.
8. Bernachy-Barbe F, Conil N, Guillot W, Talandier J. Observed heterogeneities after hydration of MX-80 bentonite under pellet/powder form. *Appl Clay Sci*. 2020;189:105542.
9. Bucher F, Müller-Vonmoos M. Bentonite as a containment barrier for the disposal of highly radioactive wastes. *Appl Clay Sci*. 1989;4(2):157-177.
10. Karnland O, Nilsson U, Weber H, Wersin P. Sealing ability of Wyoming bentonite pellets foreseen as buffer material–laboratory results. *Phys Chem Earth, Parts A/B/C*. 2008;33:S472-S475.
11. Lloret A, Villar MV, Sanchez M, Gens A, Pintado X, Alonso EE. Mechanical behaviour of heavily compacted bentonite under high suction changes. *Géotechnique*. 2003;53(1):27-40.
12. Sun H, Scaringi G, Mašín D, Najser J. An experimental investigation on the swelling behavior of compacted B75 bentonite. *Eng Geol*. 2022;296:106452.
13. Bernachy-Barbe F. Homogenization of bentonite upon saturation: density and pressure fields. *Appl Clay Sci*. 2021;209:106122.
14. Molinero Guerra A, Mokni N, Cui YJ, et al. Impact of initial structural heterogeneity on long-term swelling behavior of MX80 bentonite pellet/powder mixtures. *Can Geotech J*. 2020;57(9):1404-1416.
15. Villar MV, Iglesias RJ, Gutiérrez-Álvarez C, Carbonell B. Pellets/block bentonite barriers: laboratory study of their evolution upon hydration. *Eng Geol*. 2021;292:106272.

16. Mayor JC, García-Siñeriz JL, Alonso E, Alheid HJ, Blumbling P. Engineered barrier emplacement experiment in Opalinus Clay for the disposal of radioactive waste in underground repositories *(No. ENRESA–02/05)*. Empresa Nacional de Residuos; 2005.
17. Gens, A., Garcia-Molina, A. J., Olivella, S., Alonso, E. E., & Huertas, F. Analysis of a full scale in situ test simulating repository conditions. *International Journal for Numerical and Analytical Methods in Geomechanics*. 1998;22(7), 515-548.
18. Dupray F, François B, Laloui L. Analysis of the FEBEX multi-barrier system including thermoplasticity of unsaturated bentonite. *Int J Numer Anal Methods Geomech*. 2013;37(4):399-422.
19. Zheng L, Xu H, Rutqvist J, et al. The hydration of bentonite buffer material revealed by modeling analysis of a long-term in situ test. *Appl Clay Sci*. 2020;185:105360.
20. Garitte B, Shao H, Wang XR, et al. Evaluation of the predictive capability of coupled thermo-hydro-mechanical models for a heated bentonite/clay system (HE-E) in the Mont Terri Rock Laboratory. *Environ. Earth Sci*. 2017;76:1-18.
21. Alonso EE, Alcoverro J, Coste F, et al. The FEBEX benchmark test: case definition and comparison of modelling approaches. *Int J Rock Mech Min Sci*. 2005;42(5-6):611-638.
22. Gens A, Sánchez M, Guimarães LDN, et al. A full-scale in situ heating test for high-level nuclear waste disposal: observations, analysis and interpretation. *Géotechnique*. 2009;59(4):377-399.
23. Alonso E, Hoffmann C. Modelling the field behaviour of a granular expansive barrier. *Phys Chem Earth, Parts A/B/C*. 2007;32(8-14):850-865.
24. Dupray F, Laloui L. Numerical analysis of canister movements in an engineered barrier system. *Acta Geotech*. 2016;11(1):145-159.
25. Gens A, Alcoverro J, Blaheta R, et al. HM and THM interactions in bentonite engineered barriers for nuclear waste disposal. *Int J Rock Mech Min Sci*. 2021;137:104572.
26. Bosch JA, Ferrari A, Laloui L. Coupled hydro-mechanical analysis of compacted bentonite behaviour during hydration. *Comput Geotech*. 2021;140:104447.
27. Charlier R. *Approche unifiée de quelques problèmes non linéaires de mécanique des milieux continus par la méthode des éléments finis*. Dissertation. University of Liège; 1987.
28. Ferrari A, Bosch JA, Baryla P, Rosone M. Volume change response and fabric evolution of granular MX80 bentonite along different hydro-mechanical stress paths. *Acta Geotech*. 2022;17:3719-3730.
29. Sakaki T, Lüthi BF, Vogt T. Investigation of the emplacement dry density of granulated bentonite mixtures using dielectric, mass-balance and actively heated fiber-optic distributed temperature sensing methods. *Geomech Energy Environ*. 2022;32:100329.
30. Müller HR, Garitte B, Vogt T, et al. Implementation of the full-scale emplacement (FE) experiment at the Mont Terri rock laboratory. In: Mont Terri Rock Laboratory, 20 Years. Birkhäuser, Cham; 2018:289-308.
31. NAGRA. *Implementation of the Full-scale Emplacement Experiment at Mont Terri: Nagra Design, Construction and Preliminary Results*. Technical Report 15-02, NAGRA; 2019.
32. García-Siñeriz JL, Villar MV, Rey M, Palacios B. Engineered barrier of bentonite pellets and compacted blocks: state after reaching saturation. *Eng Geol*. 2012;192:33-45.
33. Collin F. *Couplages thermo-hydro-mécaniques dans les sols et les roches tendres partiellement saturés*. Dissertation. Université de Liège in Department ArGEnCo; 2003.
34. Collin F, Li XL, Radu JP, Charlier R. Thermo-hydro-mechanical coupling in clay barriers. *Eng Geol*. 2002;64:179-193.
35. Collin F, Chambon R, Charlier R. A finite element method for poro mechanical modelling of geotechnical problems using local second gradient models. *Int J Numer Methods Eng*. 2006;65(11):1749-1772.
36. Panday S, Corapcioglu MY. Reservoir transport equations by compositional approach. *Transp Porous Media*. 1989;4(4):369-393.
37. Ferrari A, Favero V, Marschall P, Laloui L. Experimental analysis of the water retention behaviour of shales. *Int J Rock Mech Min Sci*. 2014;72:61-70.
38. NAGRA. Modellhaftes Inventar für radioaktive Materialien MIRAM 12. *Nagra Arbeitsbericht NAB 13–39*; 2013.
39. Seiphoori A, Ferrari A, Laloui L. Water retention behaviour and microstructural evolution of MX-80 bentonite during wetting and drying cycles. *Géotechnique*. 2014;64(9):721-734.
40. Laloui L, Francois B. ACMEG-T: soil thermoplasticity model. *J Eng Mech*. 2009;135(9):932-944.
41. Nuth M, Laloui L. Effective stress concept in unsaturated soils: clarification and validation of a unified framework. *Int J Numer Anal Methods Geomech*. 2008;32(7):771-801.
42. Zhou AN, Sheng D, Sloan SW, Gens A. Interpretation of unsaturated soil behaviour in the stress–saturation space, I: volume change and water retention behaviour. *Comput Geotech*. 2012;43:178-187.
43. Villar MV. MX-80 Bentonite. Thermal-Hydro-Mechanical Characterisation Performed at CIEMAT in the Context of the Prototype Project *(No. CIEMAT–1053)*. Centro de Investigaciones Energeticas; 2005.
44. Wieczorek K, Miehe R, Garitte B. Measurement of thermal parameters of the HEE buffer materials. PEBS Deliverable D2.2-5; 2011.
45. Revil A, Lu N. Unified water isotherms for clayey porous materials. *Water Resour Res*. 2013;49(9):5685-5699.
46. Tang AM, Cui YJ, Le TT. A study on the thermal conductivity of compacted bentonites. *Appl Clay Sci*. 2008;41(3-4):181-189.
47. Dieudonne AC, Della Vecchia G, Charlier R. Water retention model for compacted bentonites. *Can Geotech J*. 2017;54(7):915-925.
48. Pusch R. Swelling pressure of highly compacted bentonite *(No. SKBF/KBS-TR–80-13)*. Svensk Kaernbraenslefoersoerjning AB; 1980.
49. Gens A. Soil–environment interactions in geotechnical engineering. *Géotechnique*. 2010;60(1):3-74.
50. Pusch R, Bluemling P, Johnson LH. Performance of strongly compressed MX-80 pellets under repository-like conditions. *Appl Clay Sci*. 2003;23:239-244.

51. Bossart P, Meier PM, Moeri A, Trick T, Mayor JC. Geological and hydraulic characterisation of the excavation disturbed zone in the Opalinus Clay of the Mont Terri Rock Laboratory. *Eng Geol*. 2002;66(1-2):19-38.
52. Crisci E, Ferrari A, Giger SB, Laloui L. Hydro-mechanical behaviour of shallow Opalinus Clay shale. *Eng Geol*. 2019;251:214-227.
53. Favero V, Ferrari A, Laloui L. Thermo-mechanical volume change behaviour of Opalinus Clay. *Int J Rock Mech Min Sci*. 2016;90:15-25.
54. Parisio F, Vilarrasa V, Laloui L. Hydro-mechanical modeling of tunnel excavation in anisotropic shale with coupled damage-plasticity and micro-dilatant regularization. *Rock Mech Rock Eng*. 2018;51(12):3819-3833.
55. Van Genuchten MT. A closed-form equation for predicting the hydraulic conductivity of unsaturated soils 1. *Soil Sci Soc Am J*. 1980;44(5):892-898.
56. Senger R, Papafotiou A, Marschall P. Thermo-hydraulic simulations of the nearfield of a SF/HLW repository during early-and late-time post-closure period. *Nagra Working Report NAB*; 2014:14-11.
57. Seiphoori A. *Thermo-Hydro-Mechanical Characterisation and Modelling of MX-80 Granular Bentonite*. Dissertation. EPF; 2014.
58. Collins IF, Kelly PA. A thermomechanical analysis of a family of soil models. *Geotechnique*. 2002;52(7):507-518.
59. Van Eekelen HAM. Isotropic yield surfaces in three dimensions for use in soil mechanics. *Int J Numer Anal Methods Geomech*. 1980;4(1):89-101.

How to cite this article: Bosch JA, Ferrari A, Leupin O, Laloui L. Modelling the density homogenisation of a block and granular bentonite buffer upon non-isothermal saturation. *Int J Numer Anal Methods Geomech*. 2023;47:1979–2002. https://doi.org/10.1002/nag.3547

APPENDIX A

The constitutive model for the behaviour of bentonite is formulated using the theory of elasto-plasticity, that is, the total strain tensor ϵ is divided into elastic strains and plastic strains:

$$\mathrm{d}\epsilon = \mathrm{d}\epsilon^e + \mathrm{d}\epsilon^p \tag{A1}$$

where the superscripts e and p denote elastic and plastic strains respectively. Elastic strains evolve as a function of the following Bishop-type stress[41]:

$$\boldsymbol{\sigma}' = \boldsymbol{\sigma} - [p_a - (p_a - p_w)\, S_r]\, \mathbf{I} \tag{A2}$$

where $\boldsymbol{\sigma}$ is the total stress tensor, p_a is the pore air pressure, p_w is the pore water pressure and S_r is the degree of saturation. The equations of the model are written in terms of the stress invariants $p' = \frac{1}{3}\,\mathrm{tr}(\boldsymbol{\sigma}')$, $q = \sqrt{3}\,J$ and $\sin(3\theta) = 3\sqrt{3}\det \mathbf{s}/2J^3$, where $\mathbf{s} = \boldsymbol{\sigma}' - p'\mathbf{I}$ and $J = \sqrt{\frac{1}{2}\mathrm{tr}(\mathbf{s}^2)}$. Likewise, the strain invariants $\epsilon_v = \mathrm{tr}(\epsilon)$ and $\epsilon_d = \sqrt{\frac{1}{3}\mathrm{tr}(\boldsymbol{\gamma}^2)}$, where $\boldsymbol{\gamma} = \epsilon - \frac{1}{3}\epsilon_v \mathbf{I}$, are defined.

The elastic strains are related to changes in the effective stress and temperature, T according to:

$$\mathrm{d}\,\epsilon_v^e = \frac{p'}{\kappa}\,\mathrm{d}p' + \frac{1}{3}\beta_{T0}\mathrm{d}T, \mathrm{d}\,\epsilon_d^e = \frac{9(1-2\nu)}{2(1+\nu)}\frac{p'}{\kappa}\mathrm{d}q(18a, b) \tag{A3}$$

where κ and ν are elastic material parameters, T_r is a reference temperature and β_{T0} is a thermo-elastic parameter.[40] The yield surface, f_Y in the stress space is[58]:

$$f_Y = q^2 - M^2\left[\alpha + (1-\alpha)\left(\frac{2p'}{p'_Y}\right)\right]^2 \left(p'_Y - p'\right)\, p' = 0 \tag{A4}$$

where M is the critical stress ratio, α is a material parameter and p'_Y corresponds to the yield pressure. M is a function of $\sin(3\theta)$[59]:

$$M\ (\theta) = M_c\left[\frac{1 + b_L \sin(3\theta)}{1 + b_L}\right]^{-0.229} \tag{A5}$$

where b_L is defined as:

$$b_L = \frac{(M_c/M_e)^{1/-0.229} - 1}{(M_c/M_e)^{1/-0.229} + 1} \tag{A6}$$

where $M_c = \frac{6\sin\phi'}{3-\sin\phi'}, M_e = \frac{6\sin\phi'}{3+\sin\phi'}$ and ϕ' is the shear strength angle at failure

The yield pressure, p'_Y depends on the degree of saturation according to:

$$\frac{p'_Y}{p'_r} = \left(\frac{p'_{TY}}{p'_r}\right)^{\frac{\lambda_s-\kappa}{\lambda(S_r)-\kappa}} \tag{A7}$$

where p'_{TY} is the saturated yield pressure at current temperature, p'_r is a reference stress, λ_s defines the elastoplastic compressibility for saturated states and $\lambda(S_r)$ is a function expressing the evolution of elastoplastic compressibility with the degree of saturation:

$$\lambda\ (S_r) = \lambda_s\ - r\,(\lambda_s - \kappa)\left(1 - S_r^{\zeta}\right)^{\xi} \tag{A8}$$

where r, ζ and ξ are material parameters. The dependency of yield on temperature is introduced after Laloui and François[40]:

$$p'_{TY} = p'_{Ys}\ \left[1 - \gamma_T \ln\left(\frac{T}{T_r}\right)\right] \tag{A9}$$

where p'_{Ys} is the hardening variable (corresponding to the yield pressure at $S_r = 1$ and $T = T_r$ for a fixed ϵ_v^p) and γ_T is a material parameter. Volumetric and deviatoric plastic strain increments are given by[58]:

$$\frac{\mathrm{d}\epsilon_d^p}{\mathrm{d}\epsilon_v^p} = \frac{q}{M^2\left(p' - p'_Y/2\right)\left[\alpha + (1-\alpha)\left(2p'/p'_Y\right)\right]^2} \tag{A10}$$

p'_{Ys} evolves according to the hardening law:

$$\frac{\mathrm{d}p'_{Ys}}{p'_{Ys}} = \frac{\mathrm{d}\epsilon_v^p}{\lambda_s - \kappa} \tag{A11}$$

The water retention model is formulated in terms of the water ratio, e_w (ratio of water volume with respect to volume of solids) which is divided into free water ratio, $e_{w,f}$ (volume of non-adsorbed water with respect to volume of solids) and adsorbed water, $e_{w,a}$ (volume of adsorbed water with respect to volume of solids), that is, $e_w = e_{w,f}\ + e_{w,a}$. The degree of saturation is computed as $S_r = e_w/e$. The evolution of free water ratio $e_{w,f}$ is modelled as:

$$e_{w,f} = \left(e - e_{w,a}\right)\ \left[1 + \left(a\left(e - e_{w,a}\right)^b s\right)^n\right]^{1/n-1} \tag{A12}$$

where n, a and b are material parameters and s stands for matric suction. $e_{w,a}$ follows a Freundlich isotherm:

$$e_{w,a} = e_{w,a}^C\ \left[\exp\left(-\frac{M_w}{\rho_{w,a}RT_r}s\right)\right]^{1/m} \tag{A13}$$

where $\rho_{w,a}$ is the density of adsorbed water, M_w is the molar mass of water, $e_{w,\,a}^C$ is the adsorption capacity parameter and m is a material parameter.